Influence of wing morphological and inertial parameters on flapping flight performance

Yufeng Chen, Kevin Ma, and Robert J. Wood

Abstract—Here we experimentally quantify the effects of wing morphological and inertial parameters on flapping flight performance. Through running at-scale, passive pitching experiments with different wing designs, we compare the relative importance of wing inertia, wing shape, and wing-actuation pairing. We find wing inertia strongly influences the coupling between stroke and pitch dynamics, which directly impacts lift production and efficiency. Flapping resonance frequency is reduced as wing aspect ratio or area moment increases. Further, wing leading edge design strongly influences chordwise center of pressure, which further impacts pitching dynamics. Based on our experimental results we propose a new wing design and measure 37% increase in mean lift relative to a previous work [1].

I. Introduction

Recent advances in micro-fabrication technology and a deeper understanding of insect flight have enabled a number of flapping wing vehicles to achieve stable hovering flight [2], [3], [4]. Compared to traditional fixed wing aircraft or rotary wing vehicles, flapping wing devices have higher maneuverability [5] and can achieve smaller physical sizes. These vehicles rely on unsteady aerodynamic phenomena such as delayed stall and vortex shedding to generate large periodic forces. At the scale of small birds, vehicles such as the Delfly and the Nanohumming bird have demonstrated autonomous flight by incorporating onboard sensors and power.

However, achieving autonomous flight becomes increasingly challenging as vehicle size shrinks and relative sensor and battery payload increase. The Harvard RoboBee [4] is an 80mg flapping wing robot that achieves hovering flight but relies on a tether to draw power from off-board amplifiers. A previous study aimed to increase payload capability by scaling up the actuator and wing size [1]. The scaled up RoboBee weighs 210mg, has a wing span of 4.2cm, and is capable of lifting 110mg of payload. Figure 1 shows a photograph of the scaled up RoboBee. While this work allows the incorporation of onboard sensors and circuitry, the vehicle still cannot carry an onboard battery. Here we take an experimental approach towards improving the robot's flapping performance and thus payload capacity.

These authors are with the School of Engineering and Applied Sciences, Harvard University, Cambridge, MA 02138, USA, and the Wyss Institute for Biologically Inspired Engineering, Harvard University, Boston, MA, 02115, USA (email: yufengchen,kevinma,rjwood@seas.harvard.edu)
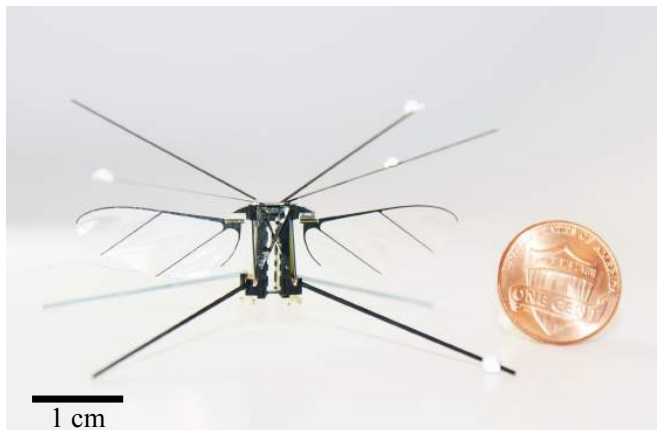
Figure 1. A recent RoboBee design weighing 210mg and capable of lifting 110mg of payload. The robot wing span is 4.2cm and operates at 70Hz.

Numerous previous studies on insect flight focus on either unsteady fluid mechanics [6], [7], [8] or influences of flapping kinematics [9], [10]. While these studies lead to useful design principles, most do not explore the influences of wing morphological and inertial parameter on flight performance. Although a quasi-steady model with passive pitching [11] has been proposed, the model relies on careful parameter fitting to a particular wing shape. In this paper, we study wing morphological and inertial parameter influence on flapping flight through designing and testing a suite of different wing and hinge pairs. We demonstrate that wing morphology has a large impact on lift enhancement and significantly changes the robot operating frequency. Through experimentation we improve the robot maximum mean lift by 37%, which is equivalent to approximately doubling the current payload capability.

Our results show wing inertia influences stroke and pitch coupling, which further impacts mean lift by more than 60%. Increasing wing aspect ratio (AR) reduces system resonance and adversely affects structural stiffness. Wing shape parameters – first area moment ($\hat{r}_1$) and leading edge sweep ratio ($LESR$) – influence passive pitching. Finally, reducing wing size increases system operation frequency and mean lift at the cost of higher power consumption. While our experimental studies aim to improve the performance of the Harvard RoboBee, the experimental results are directly applicable to other flapping wing robotic designs.
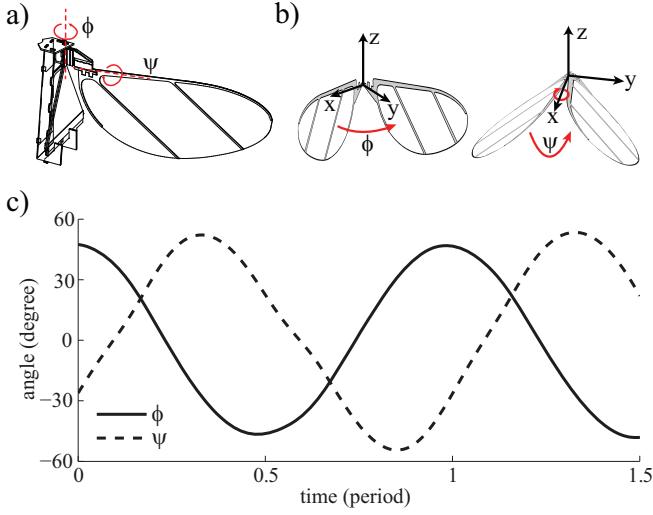
Figure 2. Flapping kinematics of the Harvard RoboBee. a) Illustration of the two rotational degrees of freedom. b) Illustration of the wing stroke (ϕ) and pitch (ψ) motion with respect to the coordinate definition. c) Example of tracked wing stroke and pitch motion. The horizontal axis is scaled to a flapping period.

II. EXPERIMENTAL SETUP

A. Flapping kinematics

As shown in figure 2a, the flapping motion has two degrees of freedom—stroke and pitch. Two piezoelectric bimorphs actuate the wing stroke motion while wing pitch is passively mediated by compliant flexures. Figure 2b defines the wing stroke angle ϕ and pitch angle ψ. Figure 2c shows both stroke and pitch motion can be approximated as pure sinusoids:

$$\begin{aligned} \phi(t) &= \phi_{\max} \cos(2\pi f t) \\ \psi(t) &= \psi_{\max} \sin(2\pi f t + \delta) \end{aligned} \quad (1)$$

where $\phi_{\max}$ is the stroke amplitude, $\psi_{\max}$ is the wing pitch amplitude, f is the flapping frequency and δ is the relative phase shift. In our experiments f is specified, whereas $\phi_{\max}$, $\psi_{\max}$, and δ depend on driving signals, wing morphological and inertial designs, actuator sizing, and wing driver transmission.

B. Wing designs and fabrication

The millimeter-scale wings consists of a carbon fiber frame and a polyester membrane. Based on Ellington's study [12] of insect wing shape and parametrization, the wing morphology is fully prescribed by a physical scale R, a dimensionless function $y_{LE}(r)$, and two dimensionless quantities $\hat{r}_1$ and AR. Here R is the wing span, $y_{LE}(r)$ is the wing leading edge profile, $\hat{r}_1$ is the dimensionless first moment of area, and AR is the aspect ratio. The inertial parameters such as mass and moment of inertia can be changed by varying carbon fiber spar thicknesses. Figure 3 illustrates the parameters we modify. Figure 3a shows how wing inertia can be changed by varying spar thickness. Figure 3b shows how varying AR changes the wing spanwise to chordwise ratio. Figure
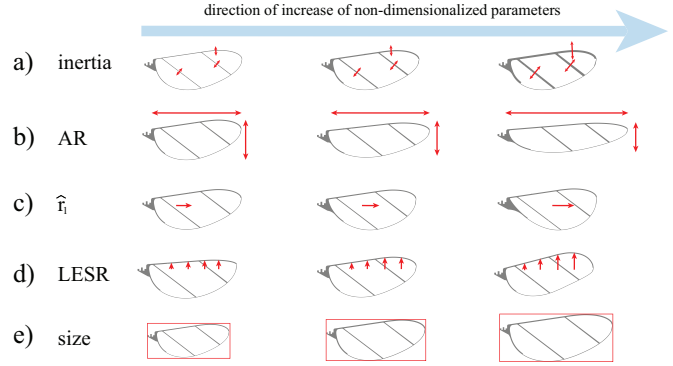

Figure 3. Illustration of different wing morphological and inertial parameters. a) Change of wing spanwise and chordwise moment of inertia by varying spar thickness from 0.14mm to 0.29mm. b) Change of aspect ratio AR from 3 to 5.5. c) Change of spanwise first wing moment $\hat{r}_1$ from 0.49 to 0.55. d) Change of leading edge sweep ratio in range of 0.5 to 1.75. e) Change of wing size from $94.5mm^2$ to $162\ mm^2$.

3c shows how varying $\hat{r}_1$ shifts wing spanwise area moment toward the wing tip. Figure 3d shows variation of the leading edge profile (LESR) by scaling it with a multiplicative factor in the range of 0.5 to 1.75. Finally, figure 3e shows how we further vary wing size to investigate actuator-wing pairing. All wing design variations are scaled relative to the "baseline" wing design from the scaled up Robobee from [13].

C. Wing driver setup

In addition to quantifying the influence of wing morphological and inertial parameters, we aim to improve the RoboBee lift capability. The scaled RoboBee utilizes a modular design such that it consists of two symmetrical halves. Here we use one half of the RoboBee as the wing driver. Specific design parameters and manufacturing methods are discussed in [13]. The wing driver is mounted on an existing setup to measure lift and drag forces. A video of the flapping wing motion is captured using a Phantom 7.0 high speed camera and post-processed to extract kinematics.

D. Motion tracking method

We develop an efficient and robust kinematic tracking method to rapidly test different wing planforms. While previous studies developed tracking methods based on area thresholding or laser sheet illumination, these methods need to be meticulously calibrated for wing shape, size, and camera lighting [9], [13]. To study wing inertia, morphology, and sizing effects on force generation and efficiency, we run more than 2000 flapping experiments for over 40 different wing designs. Every flapping experiment is recorded using a high speed camera and post processed to extract the kinematic parameters $\phi_{\max}$, $\psi_{\max}$, and δ.

Here we introduce a computationally efficient tracking method that does not require manual calibration and expensive nonlinear calculations such as morphological opening and closing. Given a sequence of raw images (Figure 5a), we
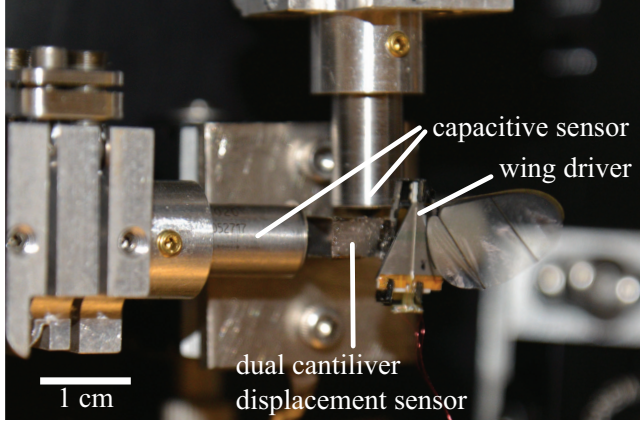
Figure 4. Illustration of the experimental set up. Two capacitive force sensors measure mean lift and drag forces. One half of the scaled up RoboBee serves as the wing driver. A high speed camera captures flapping kinematics at 10KHz, and a resistive circuit measures power dissipation.
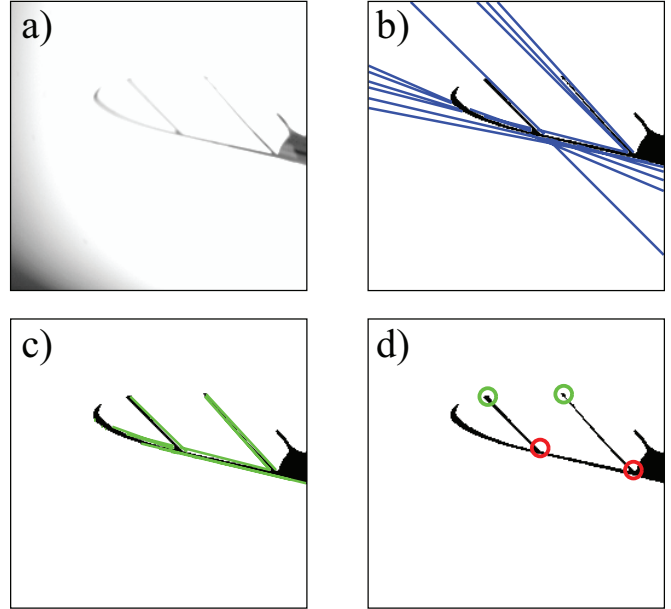

Figure 5. Automated kinematic tracking algorithm. a) The original image captured by the high speed video camera. b) Hough transform detects line segments in the picture. c) The endpoints of the Hough transformed lines are projected to the thresholded image. d) Intersection points and endpoints are computed to identify wing leading edge points and trailing edge points. These points allow the estimation of instantaneous wing stroke and pitch.

	# 1	# 2	# 3	# 4	# 5	# 6
spar width (mm)	0.14	0.17	0.20	0.23	0.26	0.29
$I_{xx}(mg{\cdot}mm^2)$	1.91	2.25	2.56	2.90	3.27	3.64
$I_{zz}(mg{\cdot}mm^2)$	40.6	48.8	57.2	65.6	73.4	82.7

Table I
INERTIAL PROPERTIES OF WINGS WITH DIFFERENT SPAR WIDTH

first remove the background and threshold the image. Next, we compute the Hough transform of the binary image to estimate major line segments. The blue lines in figure 5b show the lines found by Hough transform. These line segments terminate at the image border and may be skewed due to noise. To track the leading edge spar and two diagonal wing spars, we project the endpoints of each Hough transformed line to the closest black pixel. The green lines in figure 5c show the Hough transformed lines after the endpoints are projected to the wing skeleton. These lines accurately represent the wing leading edge spar and diagonal spars. Finally, we compute the intersection of these lines and cluster the points to identify the spar intersections. The red circles in figure 5d show the computed intersection points. Finally, we locate the diagonal spar endpoints and label them as trailing edge points. These points are labeled in green in figure 5d.

Knowing the wing geometry and having located the leading edge points (red) and trailing edge points (green), we can compute the kinematic parameter $\phi(t_i)$ and $\psi(t_i)$, where t_i represent the ith frame. The rotation matrix from a standard reference frame to the current frame is given by:

$$\begin{pmatrix} x_1 \\ y_1 \\ z_1 \end{pmatrix} = \begin{pmatrix} \cos\phi & -\cos\psi\sin\phi & -\sin\psi\sin\phi \\ \sin\phi & \cos\psi\cos\phi & \sin\psi\sin\phi \\ 0 & -\sin\psi & \cos\psi \end{pmatrix} \begin{pmatrix} x_0 \\ y_0 \\ z_0 \end{pmatrix} \tag{2}$$

Here each tracked point gives (x_1, y_1) but does not provide depth information. We formulate a non-linear overdetermined system consisting of eight equations and two unknowns. This equation can be solved by numerical least squares methods.

III. RESULTS

A. Wing inertia influence on system resonance

In flapping flight with passive pitching, stroke and pitch coupling is sensitively dependent on the effects of wing inertia [14], [15], [16]. Here we investigate the effect of

wing inertia by varying spar thickness while keeping other morphological parameters constant. Table I shows the spar thickness, spanwise and chordwise moment of inertia of the wings used in experiments. The wing spanwise and chordwise inertia increases linearly as wing index increases. We further explore wing inertial influence on system resonance. Here we model the system as a mass spring damper system and define system resonance as the flapping frequency that corresponds to maximum stroke amplitude.

While a previous study [17] predicts that a reduction of wing inertia improves performance, our result shows that the best performing wing does not have the minimum inertia. Wing spanwise and chordwise inertia affect stroke and pitch amplitude, which further affects lift production and power dissipation. Figure 6a shows the measured maximum lift from each wing. Figure 6b and 6c further shows the corresponding driving frequency and power dissipation. Figure 6a shows that wing 4 generates the highest mean lift when driven at $140Hz$ and the actuator consumes $23.1mW$ power. Figure 6b shows that the flapping resonance decreases as wing inertia
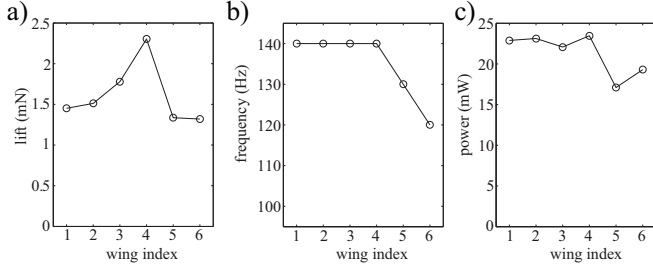
Figure 6. Wing performance versus wing spar width. a) Maximum mean lift versus wing number. b) Driving frequencies at maximum mean lift versus wing number. c) Power dissipation at maximum mean lift versus wing number.

increases. In later discussions we show how this phenomenon can be described using a non-linear spring damper system based on the quasi-steady model. Figure 6c shows that power dissipation decreases slightly as resonance frequency decreases. However, the drop in power dissipation is small compared to the reduction of mean lift.

Change of wing inertia affects wing stroke and pitch motion. Figure 7a and 7b compare the experimentally measured wing stroke amplitude of wing 1 and wing 6. As the wing driver flaps a wing with small inertia, stroke amplitude varies slowly as driving frequency changes. This suggests that the wing driver behaves as a displacement source and the wing inertial contribution is small. As wing inertia increases, stroke amplitude varies noticeably as driving frequency changes. At higher driving frequencies, wing inertial effects become significant and consequently reduce stroke amplitude. Similarly, pitching kinematics also depend on wing inertia. Figure 8a shows the measured pitching amplitude ψ for different wings when flapped at $140Hz$. The the quasi-steady model estimates $C_L \propto \sin(2\alpha) = \cos(2\psi)$, which implies that mean lift directly correlates with pitching kinematics. While Figure 6 shows that wing 4 generates the largest mean lift, Figure 8a further illustrates that wing 4 has the maximum pitch amplitude $\psi_{\max}$. Initially, $\psi_{\max}$ increases as wing inertia increases, however $\psi_{\max}$ falls sharply as wing inertia continues to increase.

We use a quasi-steady model to describe the wing inertia's effect on stroke and pitch coupling. We can formulate a system of coupled ordinary differential equation as:

$$I_{zz}\ddot{\phi} + k_1\phi + F_D R_{\text{cop,x}} = F_{act} R_{\text{cop,x}}$$
$$I_{xx}\ddot{\psi} + k_2\psi + d_2\dot{\psi} = \tau_{aero} \quad , \qquad (3)$$

where F_D is the drag force, τ_{aero} is the spanwise fluid torque, and F_{act} is the actuator input. Here we invoke the formula:

$$
\begin{aligned}
F_D &= (1.4 - \cos(2\alpha))b_1|\dot{\phi}|\dot{\phi} \\
\tau_{aero} &= b_2|\dot{\phi}|\dot{\phi}R_{\text{cop,z}} \\
F_{act} &= F_a \cos(2\pi f t)
\end{aligned}
\qquad (4)
$$

where $\alpha = \frac{\pi}{2} - \psi$ is the angle of attack. $R_{\text{cop,x}}$ and $R_{\text{cop,z}}$ are the x and z components of the center of pressure. We
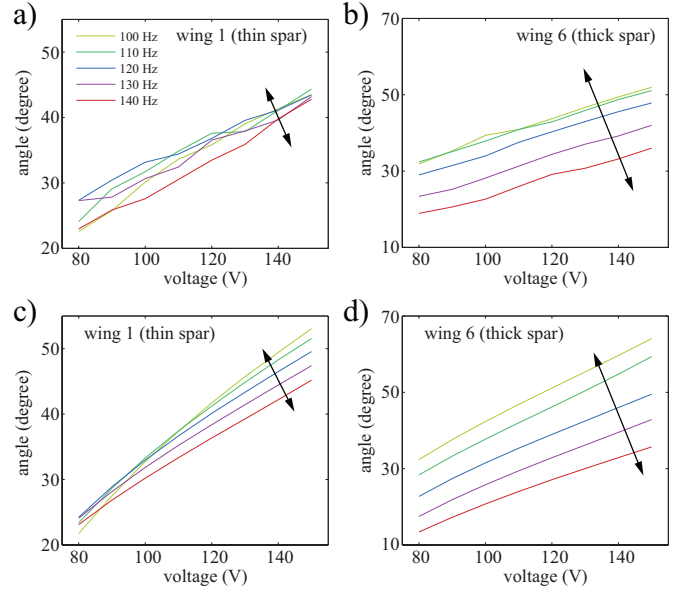

Figure 7. Influence of wing inertia on stroke amplitude $\phi_{\max}$. Each plot shows experiments or simulations with driving frequencies from $100Hz$ to $140Hz$ in steps of $10Hz$, and driving voltage amplitude from $80V$ to $150V$ in steps of $10V$. a) Experimentally measured $\phi_{\max}$ for the wing of thinnest spar width. b) Experimentally measured $\phi_{\max}$ for the wing of thickest spar width. c) Simulated $\phi_{\max}$ for the wing of thinnest spar width. d) Simulated $\phi_{\max}$ for the wing of thickest spar width.
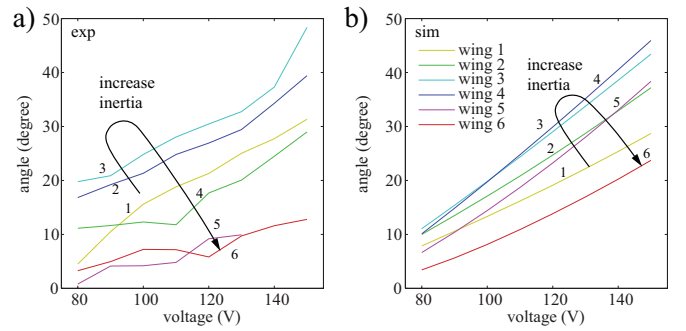

Figure 8. Influence of wing inertia on pitch amplitude $\psi_{\max}$. Each plot shows experiments or simulations with driving frequencies at $140Hz$, and driving voltage amplitude from $80V$ to $150V$ in steps of $10V$. a) Experimentally measured pitch amplitude $\psi_{\max}$ for all 6 wings at $140Hz$. b) Simulated pitch amplitude $\psi_{\max}$ for all 6 wings at $140Hz$. The arrows show maximum pitching is achieved at an intermediate wing inertia value. Resonance of pitching amplitude sensitively depends on wing inertia.

approximate $R_{\text{cop,x}}$ using the first moment of wing shape:

$$R_{\text{cop,x}} = \hat{r}_1 R. \qquad (5)$$

From a previous study we found that $R_{\text{cop,z}}$ is a strong function of α [18]. We approximate $R_{\text{cop,z}}$ using a sigmoid function:

$$R_{\text{cop,z}} = (0.25 + \frac{0.25}{1 + \exp(5 \times (1 - \frac{4}{\pi}\alpha))})\bar{c} \qquad (6)$$

Here we scale the sigmoid function such that we recover the thin airfoil limit at small α and the symmetric condition at $\alpha = \frac{\pi}{2}$. The coefficients b_1, b_2, k_1, k_2, d_2, and F_a

are manually adjusted to fit the measured data. This simple model intends to investigate the trend of inertia influence on flapping performance. It ignores unsteady effects such as added mass, wake capture and rotational acceleration because in passive pitching simulations these extra terms may lead to excessive over-fitting. Here we use the model to demonstrate how the trend observed in Figures 7 and 8 is caused by stroke and pitch coupling. Figure 7c and 7d shows the simulated stroke amplitude for wings 1 and 6. Similar to figure 7a and 7b, we observe that the stroke amplitude varies slowly with frequency for a low inertia wing and varies rapidly for a high inertia wing. Figure 8b shows simulated pitch kinematics of each wing when driven at $140Hz$. We observe a similar trend to figure 8a. Here pitch amplitude is maximum for a wing with intermediate moment of inertia.

This simplified quasi-steady model offers an intuitive description of stroke-pitch coupling. Equation (3) suggests that both stroke and pitch amplitude sensitively depend on the wing moment of inertia.

B. Wing aspect ratio influence

We investigate the influence of wing aspect ratio AR by varying this parameter while keeping wing area and spar thickness constant. Figure 9a shows the maximum mean lift as a function of AR. Figure 9b and 9c show the corresponding driving frequency and power dissipation. We observe decreasing maximum mean lift and resonance frequency as AR increases. The maximum mean lift of the wing with $AR = 3$ is slightly lower than $AR = 3.5$ because its resonance frequency is expected to be higher than $140Hz$. At the highest driving frequency and voltage ($140Hz$ and $150V$), the pitch magnitude is $36°$. We expect ψ to continue to increase at higher driving frequencies. Consequently, we expect the maximum mean lift of the wing to be the highest for the wing with smallest AR.

The reduction of resonance frequency at large AR is partially contributed by the increase of wing chordwise moment of inertia. As wing aspect ratio increases, wing radius R increases and mean chord $\bar{c}$ decreases. Consequently, the chordwise moment of inertia I_{zz} increases and the spanwise moment of inertia I_{xx} decreases. Figure 10a shows I_{zz} and I_{xx} as functions of AR. In section III.A, both experimental results and the simplified quasi-steady model demonstrate that increasing wing inertia decreases wing resonance. Here we observe that the increase in AR increases I_{zz}, which affects the resonance of the wing stroke motion. Consequently, a wing with larger AR has a lower resonance frequency.

Further, wing structural stiffness decreases rapidly as AR increases. To first order the wing bending stiffness can be modelled as that of a cantilever beam:

$$K = \frac{3EI_{zz}}{R^3}, \tag{7}$$

where E is the Young's modulus of carbon fiber and R is wing span. An increase of AR implies an increase of wing span R, and consequently leads to reduction of stiffness K. In
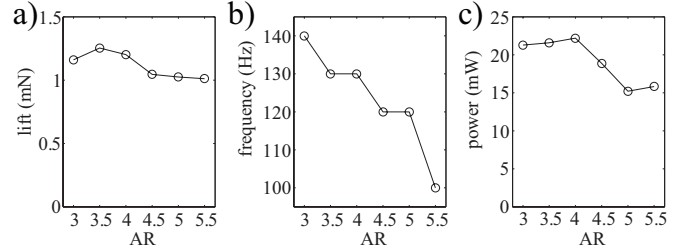

Figure 9. Wing performance versus wing aspect ratio. a) Maximum mean lift versus wing number. b) Driving frequencies at maximum mean lift versus wing number. c) Power dissipation at maximum mean lift versus wing number.

addition, the quasi-steady model predicts a quadratic increase of aerodynamic force along the wing span. Consequently, we observe the large AR wings experience significant deformation at high driving frequencies. Figure 10b compares wing deformation between $AR = 3$ and 5.5. Figure 10b-i shows a wing with $AR = 3$ being driven at $140Hz$ and $150V$. We observe the wing as a flat, rigid plate at $T = 0$ and $T = 0.15$. Figure 10b-ii shows a wing with $AR = 5.5$ being driven at $120Hz$ and $110V$. Although the operating frequency and voltage input are lower, we observe significant deformation. At $T = 0$, we observe a torsional wave propagating from wing tip to wing root. This twist is illustrated by the red arrows on figure 10b-ii. In contrast, we do not observe large twisting for the wing with $AR = 3$. At $T = 0.15$, the wing tip accelerates and the force near the wing tip quickly grows. Consequently, we observe noticeable bending of the wing leading edge spar in the $AR = 5.5$ wing. This is illustrated by the curved red line in figure 10b-ii. In contrast, the leading edge spar of the $AR = 3$ wing does not deform. This observation is illustrated by the red line segment in figure10b-i. Hence, increasing aspect ratio lowers wing resonance frequency and adversely affects the wing's structural rigidity. While some previous studies [4] indicate adequate wing flexibility improves wing performance, excessive flexibility adversely affects wing lifespan. As driving frequency and voltage continue to increase, wing deformation increases and eventually the wing leading edge spar breaks under excessive aerodynamic loading.

C. Influence of wing area moment

In the previous section we observe that increasing wing AR increases wing spanwise center of pressure and moment of inertia. Increasing I_{zz} leads to a reduction of the flapping resonance frequency and adversely impacts structural stiffness. Here we investigate the effect of increased spanwise center of pressure without significantly changing the moment of inertia. This can be done by varying the first area moment $\hat{r}_1$ while holding other wing morphological parameters constant. Figure 11 compares the performance of wings with $\hat{r}_1$ in the range of 0.49 to 0.55. Figure 11a shows that mean lift increases as $\hat{r}_1$ increases. Unlike the
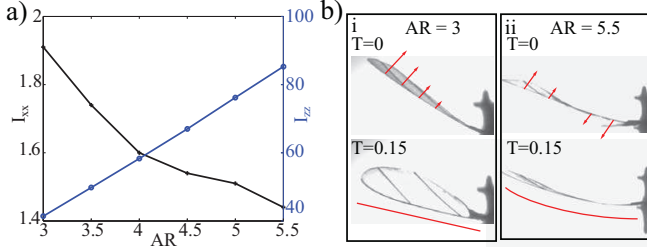
Figure 10. Aspect ratio influence on flapping performance. a) Wing spanwise and chordwise moment of inertia as functions of aspect ratio. As AR increases, I_{xx} decreases and I_{zz} increases. b) Aspect ratio influence on structural stiffness. b-i) shows the wing with small aspect ratio (AR=3) has sufficient structural stiffness. There is not a noticeable torsional wave along the wing span during pitch rotation at wing period T=0. The wing leading edge spar is straight at $T = 0.15$ as wing stroke velocity increases. b-ii) shows that the wing with a large aspect ratio (AR=5.5) has reduced structural stiffness. There is a significant torsional wave along wing span during pitching at T=0. The wing leading edge spar bends noticeably at $T = 0.15$ as the wing stroke velocity increases.
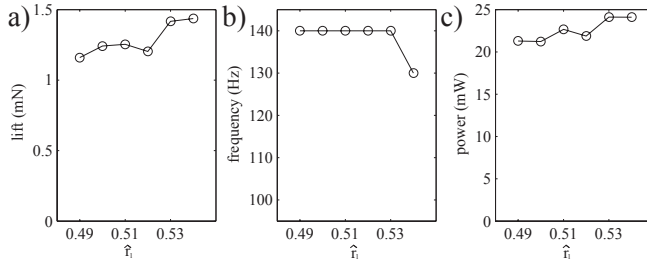

Figure 11. Wing performance versus wing first moment of area $\hat{r}_1$. a) Maximum mean lift versus wing number. b) Driving frequencies at maximum mean lift versus wing number. c) Power dissipation at maximum mean lift versus wing number.

trend shown in figure 9b, figure 11b shows that the flapping resonance frequency remains at $140Hz$ except for $\hat{r}_1 = 0.54$. The wing with $\hat{r}_1 = 0.54$ has a resonance frequency at $130Hz$ because it experiences large deformation at $140Hz$ due to the large aerodynamic loading. Figure 11c shows that power dissipation increases slowly as mean lift increases.

Here, flapping resonance frequency changes slowly because the change in wing inertia is small. Figure 12a shows the spanwise and chordwise moment of inertia as functions of $\hat{r}_1$. From $\hat{r}_1 = 0.49$ to $\hat{r}_1 = 0.55$ the relative change of I_{xx} and I_{zz} is less than 15%. The increase of mean lift due to increased $\hat{r}_1$ can be explained by quasi-steady scaling. Equations (11) and (12) from [17] give

$$F_L = \frac{1}{2}\rho\frac{R^4}{AR}\frac{1}{2}\tilde{C}_L w^2 \phi_{max}^2 \hat{r}_2^2, \tag{8}$$

where

$$\tilde{C}_L = C_{Lmax}\frac{2}{\pi}\int_0^\pi \sin(2\alpha)\cos^2(t)dt. \tag{9}$$

Here the quasi-steady model suggests that mean lift is proportional to $\hat{r}_2^2$. From Ellington's wing shape parametrization
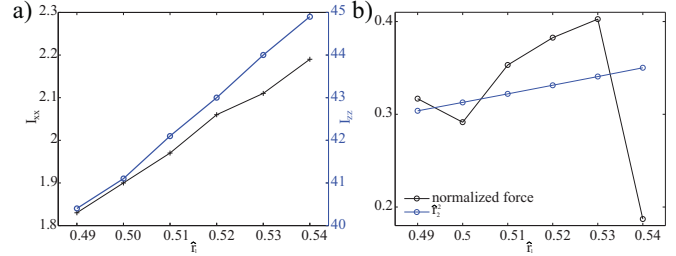

Figure 12. Inertial properties and normalized lift as functions of $\hat{r}_1$. a) Both I_{xx} and I_{zz} increase slowly as $\hat{r}_1$ increases. Here I_{xx} and I_{zz} increase by less than 15%. b) Normalized force and $\hat{r}_2^2$ as functions of $\hat{r}_1$. The quasi-steady scaling predicts that mean lift is proportional to $\hat{r}_2^2$. Here we observe a similar trend although there is noticeable deviation that may be caused by more influential parameters such as wing inertia.

study, wing first and second moments $\hat{r}_1$ and $\hat{r}_2$ are related by the empirical function:

$$\hat{r}_2 = 0.929(\hat{r}_1)^{0.732}. \tag{10}$$

Figure 12b compares the normalized force $\frac{F_L}{\frac{1}{2}\rho\frac{R^4}{AR}\frac{1}{2}\tilde{C}_L w^2 \phi_{max}^2}$ and $\hat{r}_2^2$ as functions of $\hat{r}_1$. We observe that the normalized force roughly follows the quasi-steady scaling relationship $\hat{r}_2^2$. The wing with $\hat{r}_1 = 0.54$ is an outlier because its motion has large stroke and pitch amplitudes, and consequently leads to noticeable wing deformation.

D. Leading edge sweep ratio (LESR) influence on wing pitching

We further explore the effect of wing leading edge sweep ratio on wing performance. There is noticeable spanwise flow along the leading edge of a flapping and rotating wing. As shown in 3D-CFD simulations, positive wing leading edge sweep can facilitate the growth of a wing tip vortex that enhances lift. However, varying LESR changes the chordwise center of pressure, which affects wing pitching. Here we vary the wing leading edge profile by changing the sweep ratio from 0.5 to 1.75 in steps of 0.25. Figure 13a shows that mean lift decreases monotonically as sweep ratio increases. Figure 13b shows that flapping resonance frequency is unaffected by changes in the wing sweep. Figure 13c shows small changes of power dissipation as wing sweep ratio increases.

We use quasi-steady scaling to describe the wing sweep influence on pitching dynamics. Figure 14a shows wing spanwise and chordwise moment of inertia as functions of leading edge sweep ratio. The variation of I_{xx} and I_{zz} are less than 15% and consequently the effect of changing wing inertia is small. Figure 14b shows stroke and pitch amplitude as a function of leading edge wing sweep ratio. Except the wing with the smallest wing sweep, the stroke amplitude (black) changes slowly as sweep ratio increases. In contrast, the measured pitch amplitude ψ_{max} is very sensitive to wing sweep. We observe that ψ_{max} monotonically decreases from $60°$ to $7°$. This reduction in wing pitch can be explained
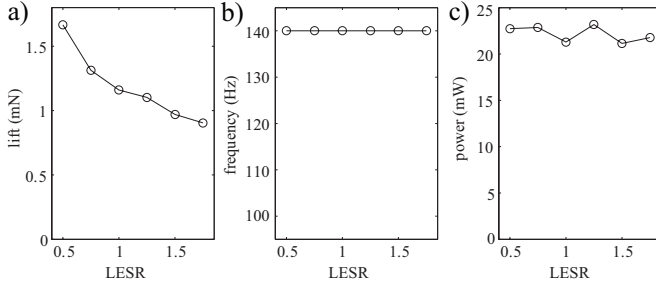
Figure 13. Wing performance versus leading edge sweep ratio. a) Maximum mean lift versus wing number. b) Driving frequencies at maximum mean lift versus wing number. c) Power dissipation at maximum mean lift versus wing number.
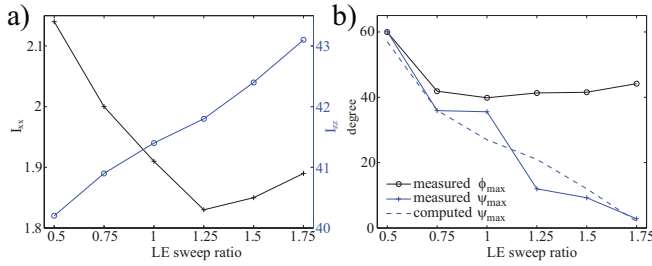

Figure 14. Leading edge sweep ratio influence on flapping performance. a) Both I_{xx} and I_{zz} vary slowly as LE sweep ratio increases. b) Measured stroke and pitch amplitude $\phi_{\max}$ and $\psi_{\max}$. We also show predicted $\psi_{\max}$ based on measured stroke kinematics using the quasi-steady model. Both the quasi-steady model and the measurement show that increased LES leads to decreased $\psi_{\max}$.

using a quasi-steady model at mid-stroke. At mid-stroke, we impose

$$K\psi + I_{xx}\ddot{\psi} = \tau_f \tag{11}$$

where K is the wing hinge stiffness, I_{xx} is the spanwise moment of inertia, and τ_f is the aerodynamic pitch torque. At mid-stroke, τ_f is given by

$$\tau_f = 2\pi^2 \rho f^2 \phi_{max}^2 \int_0^R r^2 c(r) C_f \left(r_{cop}(r,\alpha) - y_{LE}(r)\right) dr. \tag{12}$$

Here the force coefficient C_f is given by

$$C_f = \left(C_L(\alpha)\cos\alpha + C_D(\alpha)\sin\alpha\right).$$

C_L, C_D, and the local chordwise center of pressure r_{cop} can be calculated based on the method discussed in section III.A. Given the relationship $\psi = \pi/2 - \alpha$, the only unknown in equation (12) is ψ. This nonlinear equation can be solved numerically to estimate $\psi_{\max}$. We use the measured stroke amplitude, flapping frequency, hinge stiffness, and wing shape as inputs to solve for $\psi_{\max}$. The result is shown as the dotted blue line in Figure 13b. Here the quasi-steady estimation gives the same trend as the experimental measurement.

E. Wing-actuator pairing

The current enlarged RoboBee is designed using scaling analysis that does not consider wing-actuator pairing. Here we investigate wing-actuator pairing by varying wing size. Changing wing size has a large impact on wing inertia and system resonance frequency. A previous study [4] shows system resonance frequency can be approximated by the formula

$$f = \sqrt{\frac{k_{eq}}{T^2 I_{zz}}}, \tag{13}$$

where k_{eq} is the effective stiffness and T is the robot transmission ratio. k_{eq} is determined by the geometry and material property of compliant flexures and T is defined to be the ratio between stroke motion output and actuator tip displacement. This transmission ratio T is determined by the laminate material thickness. While it is possible to vary these parameters in the wing driver designs, it is practically difficult to build and test many wing drivers to study system resonance. Here we can easily study resonance by varying the wing inertial parameter I_{zz}.

Changes in wing spanwise moment of inertia directly impacts resonance frequency since I_{zz} is proportional to R^4. This implies

$$f \propto \frac{1}{R^2}. \tag{14}$$

Equation (14) suggests that a decrease of wing size increases resonance frequency. From a system level perspective, changing wing radius also influences the net force output. The RoboBee uses a four-bar linkage [5] that can be modeled as

$$F_D = F_{act} \frac{L_3}{R_{\text{cop,x}}} \tag{15}$$

where F_{act} is the force output from the actuator, $R_{\text{cop,x}}$ is the spanwise center of pressure and L_3 is the effective effort arm length of the lever-like transmission.. Assuming the magnitude of the output force F_{act} is limited by electro-mechanical properties of the piezoelectric actuator, equation (15) implies reducing the spanwise wing center of pressure $R_{\text{cop,x}}$ increases the amount of drag force F_D an actuator can drive against. Since the lift and drag forces are positively correlated, equations (15) suggest that reducing wing size leads to increased mean lift force.

However, reducing wing size also has negative effects. Firstly, the robot flexural transmission life time decreases as operating frequency increases. In addition, both aerodynamic efficiency and robot power dissipation increase as wing size shrinks and flapping frequency increases. Consider two different sized wings that operate at different frequencies to generate identical lift. Equation (8) suggests

$$R_1^4 f_1^2 = R_2^4 f_2^2 \tag{16}$$

This relationship implies $\frac{1}{R^2} \propto f$. The aerodynamic efficiency is proportional to

$$\frac{\bar{F}_L}{\bar{P}_{aero}} \propto \frac{\bar{C}_L}{\bar{C}_D R f} \propto \frac{\bar{C}_L R}{\bar{C}_D} \tag{17}$$

	wing 1	wing 2	wing 3	wing 4
wing area (mm^2)	162	135	108	94.5
F_L (mN)	1.11	1.54	1.72	2.03
$f_{resonance}$ (Hz)	70	100	130	150
P_{aero} (mW)	23.7	31.9	40.7	54.8

Table II
WING SIZE, MAXIMUM MEAN LIFT, FLAPPING RESONANCE FREQUENCY,
AND POWER DISSIPATION

In the last step of equation (17) we use the proportionality relationship between R and f. Consequently, lift per unit power decreases as wing span decreases.

To validate this system level scaling analysis, we make four wings of varying wing size and test their performance. Table II reports wing size, maximum mean lift, flapping resonance frequency and power dissipation. We observe that mean lift, flapping resonance frequency, and power dissipation increase as wing size is reduced. The qualitative relationship between flapping frequency and wing span is reported in a previous biological study [19].

F. Enhanced lift of a new wing design

Our experiments show wing size and inertia have the most significant impact on lift enhancement. Consequently, we design a new wing with smaller wing size and slightly thinner wing spars. Compared to the original wing, the wing span is reduced by 25% and the spanwise moment of inertia is reduced by 76%. In flapping experiments, we find the resonance frequency of the new wing to be $150Hz$. The wing produces $2.48mN$ mean lift when driven at $190V$ and the actuator consumes $36.5mW$ power. The resonance frequency of the original wing is $80Hz$. This wing produces $1.81mN$ mean lift when driven at $250V$ and the actuator consumes $21.5mW$. The new wing produces 37% more lift and costs 70% more power dissipation. Although this result implies the new wing is less efficient, it significantly improves mean lift without modifying actuator sizing and robot transmission. In addition, the robot operational voltage is significantly lowered, which gives much larger voltage margin for aerodynamic control and greater efficiency of the drive electronics.

IV. CONCLUSION

Here we experimentally studied the influence of wing morphological and inertial parameters on mean lift generation and power consumption. We designed and fabricated a suite of different wings and test their efficiency with an at-scale robotic flapper. The experimental study is complemented with quasi-steady models that explain the trends observed in our experiments. Finally, the experimental results lead to the design of a new wing that generate 37% more lift compared to the old wing. This is equivalent to doubling the robot payload capability and is a major improvement towards flight autonomy.

V. ACKNOWLEDGMENT

REFERENCES

[1] K. Ma, P. Chirarattananon, and R.J. Wood, Design and fabrication of a robotic flying insect for control autonomy, IEEE/RSJ Int. Conf. on Intelligent Robots and Systems, Hamburg, Germany, 2015.

[2] De Croon, G. C. H. E., et al. "Design, aerodynamics, and vision-based control of the DelFly." International Journal of Micro Air Vehicles 1.2 (2009): 71-97.

[3] Keennon, Matthew, et al. "Development of the nano hummingbird: A tailless flapping wing micro air vehicle." 50th AIAA Aerospace Sciences Meeting Including the New Horizons Forum and Aerospace Exposition, Nashville, TN. January. 2012.

[4] Ma, Kevin Y., et al. "Controlled flight of a biologically inspired, insect-scale robot." Science 340.6132 (2013): 603-607.

[5] Chirarattananon, Pakpong, Kevin Y. Ma, and Robert J. Wood. "Adaptive control of a millimeter-scale flapping-wing robot." Bioinspiration & biomimetics 9.2 (2014): 025004.

[6] Dickinson, Michael H., Fritz-Olaf Lehmann, and Sanjay P. Sane. "Wing rotation and the aerodynamic basis of insect flight." Science 284.5422 (1999): 1954-1960.

[7] Lentink, David, and Michael H. Dickinson. "Rotational accelerations stabilize leading edge vortices on revolving fly wings." Journal of Experimental Biology 212.16 (2009): 2705-2719.

[8] Cheng, Bo, et al. "Three-dimensional vortex wake structure of flapping wings in hovering flight." Journal of The Royal Society Interface 11.91 (2014): 20130984.

[9] A.L. Desbiens, Y. Chen, and R.J. Wood, A wing characterization method for flapping-wing robotic insects, IEEE/RSJ Int. Conf. on Intelligent Robots and Systems, Tokyo, Japan, Nov., 2013.

[10] MLA Bos, Frank M., et al. "Influence of wing kinematics on aerodynamic performance in hovering insect flight." Journal of fluid mechanics 594 (2008): 341-368.

[11] Whitney, J. P., and R. J. Wood. "Aeromechanics of passive rotation in flapping flight." Journal of Fluid Mechanics 660 (2010): 197-220.

[12] Ellington, C. P. "The aerodynamics of hovering insect flight. I. The quasi-steady analysis." Philosophical Transactions of the Royal Society B: Biological Sciences 305.1122 (1984): 1-15.

[13] N. Gravish, Y. Chen, S. Combes, and R.J. Wood, High-throughput study of flapping wing aerodynamics for biological and robotic applications, IEEE/RSJ Int. Conf. on Intelligent Robots and Systems, Chicago, IL, Sept. 2014.

[14] Lentink, David, Stefan R. Jongerius, and Nancy L. Bradshaw. "The scalable design of flapping micro-air vehicles inspired by insect flight." In Flying Insects and Robots, pp. 185-205. Springer Berlin Heidelberg, 2010.

[15] Kang, Chang-kwon, and Wei Shyy. "Passive Wing Rotation in Flexible Flapping Wing Aerodynamics." 30th AIAA Applied Aerodynamics Conference 2012. 2012.

[16] Zhang, Jie, Nan-Sheng Liu, and Xi-Yun Lu. "Locomotion of a passively flapping flat plate." Journal of Fluid Mechanics 659 (2010): 43-68.

[17] J.P. Whitney and R.J. Wood, Conceptual design of flapping-wing micro air vehicles, Bioinspiration and Biomimetics, vol. 7, no. 036001, 2012.

[18] Y, Chen, Gravish, N, Desbiens, A.L, Malka, R., and Wood, R.J. Aerodynamic performance of a flapping and passively rotating wing in insect flight. J. Fluid. Mech. 2015.

[19] San Ha, Ngoc, et al. "Relationship between wingbeat frequency and resonant frequency of the wing in insects." Bioinspiration & biomimetics 8.4 (2013): 046008.